Spectrochimica Acta Part A: Molecular and Biomolecular Spectroscopy 115 (2013) 516–527

Contents lists available at SciVerse ScienceDirect

Spectrochimica Acta Part A: Molecular and Biomolecular Spectroscopy

journal homepage: www.elsevier.com/locate/saa

# Investigation of interaction of nuclear fast red with human serum albumin by experimental and computational approaches

Mohammad-Bagher Gholivand [a,*], Ali R. Jalalvand [a,b], Hector C. Goicoechea [c], Mehdi Omidi [a]

[a] Department of Analytical Chemistry, Faculty of Chemistry, Razi University, Kermanshah 671496734, Iran
[b] Quality Control Laboratory, Kermanshah Oil Refining Company, Kermanshah, Iran
[c] Laboratorio de Desarrollo Analítico y Quimiometría (LADAQ), Cátedra de Química Analítica I, Universidad Nacional del Litoral, Ciudad Universitaria, CC 242, S3000ZAA Santa Fe, Argentina

## HIGHLIGHTS

- Experimental approaches including UVvis, F, DPV, LSV, and CV were applied.
- The experimental data was augmented and resolved by MCR–ALS.
- Binding of NFR to HSA was modeled by molecular modeling and MD simulations.
- The results of experimental and computational approaches were compatible.
- The obtained results suggested that the NFR binds mainly to the sub-domain IIA of HSA.

## GRAPHICAL ABSTRACT

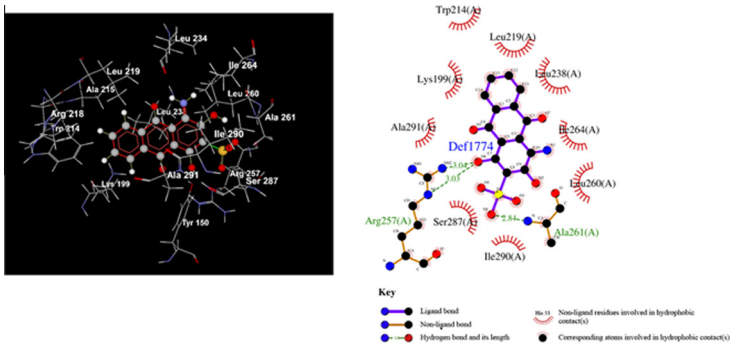


## ARTICLE INFO

*Article history:*
Received 10 March 2013
Received in revised form 6 June 2013
Accepted 12 June 2013
Available online 29 June 2013

*Keywords:*
Nuclear fast red
Human serum albumin
Voltammetry
Spectroscopy
Computational approaches

## ABSTRACT

For the first time, interaction of nuclear fast red (NFR) with human serum albumin (HSA) was studied by experimental and computational approaches. Firstly, experimental measurements including fluorescence spectroscopy (F), UVvis spectrophotometry (UVvis), cyclic voltammetry (CV), differential pulse voltammetry (DPV) and linear sweep voltammetry (LSV) were separately used to investigate the interaction of NFR with HSA and interesting thermodynamics information was obtained from these studies. Secondly, new information including electrochemical behavior of NFR–HSA complex species, relative concentrations of the various reacting species and effects of NFR on the sub-structure of HSA was obtained by applying multivariate curve resolution–alternating least squares (MCR–ALS). In this case, a row- and column-wise augmented matrix was built with DPV, LSV, F and UVvis sub-matrices and resolved by MCR–ALS. Surprisingly, by this method two NFR–HSA complex species with different stoichiometries and different electrochemical behaviors were found. Furthermore, by the use of the recorded voltammetric and spectroscopic data the binding constants of complex species were computed by EQUISPEC (a hard-modeling algorithm). Finally, the binding of NFR to HSA was modeled by molecular modeling and molecular dynamics (MD) simulations methods. Excellent agreement was found between experimental and computational results. Both experimental and computational results suggested that the NFR binds mainly to the sub-domain IIA of HSA.



* Corresponding author. Tel.: +98 831 4274557; fax: +98 831 4274559.
*E-mail address:* mbgholivand@yahoo.com (M.-B. Gholivand).

1386-1425/$ - see front matter © 2013 Elsevier B.V. All rights reserved.
http://dx.doi.org/10.1016/j.saa.2013.06.044

## Introduction

Studying interactions of small molecules to biomacromolecules such as protein or DNA is crucial for understanding many biological processes at the molecular level. Many small molecules like drugs, dyes, etc. bind to cellular serum proteins or DNA to exert their adverse and normal functions and a large number of studies have been recently undertaken in this direction [1–4].

Anthraquinone dyes are extremely resistant to biodegradation owing to their fused aromatic structures, thus they have progressively allured crucial attention from toxicological and environmental points of view, especially in light of the current increase in their applications. However, little information concerning their hazards to human has yet been accumulated, so, with the consideration of human health, the examination on the correlation of anthraquinones and toxicity was required. Nuclear fast red (NFR, Fig. S1, Supplementary data) is a typical anthraquinone dye, and as general anthraquinones, was often served as the counterstain in many biological experiments. While little attention has been paid to the biological influence of this dye, especially its binding properties with the biological macromolecules such as proteins and nucleic acid were even less.

Structurally, human serum albumin (HSA) is a non-glycosylated consisting of a single peptide chain of 585 amino acids and consists of three homologous domains, namely, I (residues 1–195), II (196–383), and III (384–585), each domain being divided into sub-domains A and B, and the overall structure is stabilized by 17 disulfide bridges [5]. The specific physiological activity of the aromatic and heterocyclic ligands upon complexation with serum albumin originates from the presence of two hydrophobic pockets in sub-domains IIA (site I) and IIIA (site II) [6]. HSA contains a single intrinsic tryptophan residue at position 214 in domain IIA, where a large hydrophobic cavity is present, and its fluorescence is sensitive to the ligands bonded nearby [7].

In general, the common methods used to investigate the interaction of proteins with small molecules include: UVvis spectrophotometry [8], FT-IR [9], electrochemistry [10], capillary electrophoresis [11], HPLC [12], and NMR [13] among others; some of these methods have been used to investigate the interaction of small molecules with biopolymers with the aid of chemometrics [14–19]. Fluorescence and UVvis spectroscopies can provide valuable qualitative and quantitative information about the binding of ligands to serum albumin and the estimation of binding constants, respectively. In general, electrochemical analysis is simple, easily implemented, low costing and fast; as well, electrochemical data can contribute to the elucidation of the interaction of small molecules with biomolecules.

By the use of the augmented matrix methods it is possible to combine data matrices of analyte profiles derived from different analytical methods. In general, the results of such approaches have indicated that the increased information in the augmented matrix improves data analysis and subsequent interpretation of the results [20]. However, combination of data matrices derived from very different analytical techniques e.g. voltammetry and spectroscopy, which monitor different properties of the analytes in the system, are much less common. It is this area of analysis, which is explored in the present investigation by the use of voltammetry and spectroscopy for the analysis of interaction of NFR with HSA.

The main objectives of this study were:

(I) We have employed experimental and computational approaches, in an attempt to determine where and how NFR binds to HSA under physiological conditions.
(II) Experimental measurements including CV, DPV, LSV, F and UVvis were used separately and in combination to obtain different information about the mentioned interaction as well as the thermodynamic parameters involved.
(III) To evaluate the results of experimental section molecular docking and MD simulations methods were used to investigate the interaction of NFR with HSA as well.

Literature survey revealed that no attempt has been made to study the interaction of NFR with HSA till date.

## Theoretical background

The MCR–ALS is one of the most versatile methods capable of resolving the system completely without assuming any model for the change in the concentration of components during the process. The MCR–ALS resolves any black system and applying appropriate constraints in reaching a better resolution is helpful. The MCR–ALS analysis decomposes the data matrix **D** into a matrix of pure concentration profiles, **C**, and a matrix of pure signals profiles, $\mathbf{S^T}$, related to the different involved species in the studied system. The product $\mathbf{CS^T}$ reconstructs the original data matrix **D** with the optimal fit, i.e., gives the minimum residual error, **E**:

$$\mathbf{D} = \mathbf{CS^T} + \mathbf{E} \quad (1)$$

The general steps in the application of MCR–ALS to any kind of data set are as follows:

1. Determination of the number of components in **D** (e.g. by singular value decomposition, SVD).
2. Building initial estimates of the **C** matrix (e.g. using evolving factor analysis, EFA). The EFA has been designed as a chemometric tool to monitor chemical processes [21,22]. The evolution of a chemical system is gradually known by recording a new response vector at each stage of the process under study. Mimicking the experimental protocol, EFA performs subsequent principal component analysis (PCA) on gradually increasing submatrices in the process direction, enlarged by adding one new row (response) at a time. This procedure is performed from top to bottom of the data set (forward EFA) and from bottom to top (backward EFA) to investigate the emergence and the decay of the process contributions, respectively. For a system with n significant components, the profile of the first contribution is obtained combining the line of the 1st s.v. of the forward EFA plot and the line of the *n*th s.v. of the backward EFA plot (related to the first contribution disappearing); the profile of the second contribution relates the line of the 2nd s.v. in the forward EFA plot to the line of the $(n-1)$th s.v. backward EFA plot, and so forth. In general, each element in the derived concentration profile is selected as the smallest value between the forward and backward s.v. lines to be combined [23]. The EFA was basically designed to work with full rank data sets and a system should fulfil the condition of full rank to be successfully analyzed by EFA. Rank deficiencies can be broken by matrix augmentation in the rank-deficient direction (C and S directions in this study) [15].
3. Given **D** and **C**, least-squares calculation of $\mathbf{S^T}$ under suitable constraints.
4. Given **D** and $\mathbf{S^T}$, least-squares calculation of **C** under suitable constraints.
5. Going back to step 3 until convergence is achieved. The convergence criterion in the MCR–ALS optimization is based on the comparison of the lack of fit (lof) obtained in two consecutive iterations. When the relative difference in fit is below a threshold value, the optimization is finished. The lof is calculated according to the expression:

$$\text{lof} = \sqrt{\frac{\sum_{ij} d_i^* - d_{ij}}{\sum_{ij} d_{ij}^2}} \quad (2)$$

where $d_{ij}$ is an element of the experimental matrix **D** and $d_{ij}^*$ the element of the MCR–ALS reproduced matrix **D**$^*$. Standard deviation of the residuals, $\sigma$, which should be similar to the error linked to the experimental measurements is expressed by the equation:

$$\sigma = \sqrt{\frac{\sum_{ij} (d_{ij}^* - d_{ij})^2}{n}} \quad (3)$$

where $n$ is the number of elements in the data set. A maximum number of iterative cycles may also be used as a stopping criterion [24].

## Experimental

### *Chemicals and solutions*

HSA (lyophilized powder, essentially globulin free, ⩾99%), NFR, warfarin (Wr) and ibuprofen (Ip) were purchased from Sigma Aldrich (St. Louis, MO, USA) and used without further purification. Stock solutions of $10^3$ μM HSA and $10^3$ μM M NFR were prepared by exact weighing and dissolution of their solid powder in a Tris–HCl 0.1 M buffer solution of pH 7.4 containing 0.1 M sodium chloride (to maintain the ionic strength of solution) and were kept at dark in a refrigerator. Working solutions of HSA or NFR were prepared by appropriate dilution of their stock solutions. Dilutions of the stock solutions in Tris–HCl buffer were preformed immediately before use. Stock solutions of Wr and Ip ($10^3$ μM) were prepared by dissolving appropriate amount of the drugs in DMSO and kept in a refrigerator. All experimental solutions were adjusted with the Tris–HCl buffer to pH 7.4. Other chemicals were analytical grade reagents and doubly distilled water was used throughout.

### *Instruments and softwares*

All fluorescence spectra were measured on a FP-6500 177 spectrofluorometer (JASCO, Japan) equipped with a thermostatic bath and a 1.0 cm quartz cuvette. The UVvis spectra were measured on an Agilent 8453 UVvis Diode-Array spectrophotometer controlled by the Agilent UVvis ChemStation software. Electrochemical experiments were performed using an Autolab modular electrochemical system (Eco Chem. Utrecht, The Netherlands) equipped with PSTA 20 model and driven by Nova 1.8 software. A conventional three-electrode cell was used with a saturated calomel electrode (SCE) as reference electrode, a Pt wire as counter electrode and a glassy carbon electrode (GCE) as working electrode. A JENWAY-3345 pH-meter was applied for the pH measurements. The chemical structure of the NFR was constructed by Hyperchem package 8.0. The molecular docking Arguslab 4.0.1 program [25] was employed to generate a docked conformation of NFR with HSA. LIGPLOT [26], a program for automatically plotting protein–ligand interactions, was used for analyzing the interactions between NFR and HSA. The MD simulations were performed using GROningen MAchine for Chemical Simulations (GROMACS) 4.5.1 package [27,28]. The MCR–ALS was implemented using the graphical interface provided by Prof. Tauler in his web page [29]. The recorded experimental data was smoothed, when necessary, and converted to matrices by means of several homemade MATLAB programs. A simple homemade MATLAB program was used for computing the concentrations of NFR and HSA and their ratio in all voltammetric and spectroscopic experiments. All calculations except MD simulations were run on a DELL XPS laptop (L502X) with Intel Core i7-2630QM 2.0 GHz, 8 GB of RAM and Windows 7–64 as its operating system. The MD simulations were performed on a computer with a Linux Fedora 15 as its operating system.

## Procedures

### *Spectroflourimetric experiments at different temperatures*

The concentration of HSA was kept constant (4.17 μM) throughout, and NFR was added to this solution in the range of 0.00–16.70 μM. The well-mixed solutions were allowed to stand for 10 min before spectroscopic measurements. The fluorescence emission spectra were recorded over a wavelength region of 290–540 nm ($\lambda_{ex}$ of 280 nm) at temperatures of 298, 304 and 310 K. It should be noted that, in the course of increasing concentrations of NFR, an instrumental inner filter effect (IFE) caused some decrease in the fluorescence emission intensity. This effect is an inherent problem of many fluorimetric procedures which lead to the results depart from the initial linearity and must be taken into account. Thus, the fluorescence intensities were corrected for absorption of exciting light and reabsorption of the emitted light to decrease the inner filter effect according to the following relationship [30]:

$$F_{Cor} = F_{Obs} \exp[(A_{ex} + A_{em})/2] \quad (4)$$

where $F_{Cor}$ and $F_{Obs}$ are corrected and observed fluorescence intensities, respectively, and $A_{ex}$ and $A_{em}$ are the absorption of the NFR at the excitation and the emission wavelengths, respectively. The intensity of fluorescence used in this study is the corrected fluorescence intensity.

### *Site selectivity of binding NFR to HSA*

To identify the binding site location of NFR on the region of HSA, the competitive experiment was carried out using two site markers. Wr, an anticoagulant drug, is a well-known marker of site I (hydrophobic sub-domain IIA) of HSA [31] and Ip, a nonsteroidal anti-inflammatory agent, has been considered as a stereotypical ligand for Sudlow's sites II (sub-domain IIIA) of HSA [32].

The site marker (Wr or Ip) was added to a mixture of NFR–HSA ([NFR]/[HSA] = 4) in the range of 0.00–16.00 μM. The percentage of the initial fluorescence due to the fluorescent probe was calculated as: (fluorescence in the presence of added site marker, $F_2$)/(fluorescence in the absence of site marker, $F_1$) × 100 and plotted versus[Site marker]/[HSA]. This plot was used to interpret the site selectivity of binding NFR to HSA.

### *Cyclic voltammetric experiments on the GCE*

Concentration of NFR was kept at 90.90 μM and HSA was added at different concentrations in the range of 0.00–90.90 μM. Each given NFR–HSA solution was stirred for 30 s and then the CV experiment was performed.

The CVs of NFR at different pH values (2–12) and also at different scan rates (ν) were recorded to obtain some information.

### *Preparation of HSA–GCE*

The GCE was first polished with 0.3 and 0.05 μm alumina slurry, and sonicated in ethanol and water successively. Films of HSA were formed on the GCE surface by transferring a droplet of 3 μl of 4 mg ml$^{-1}$ HSA solution onto its surface and allowing the electrode to dry. It was then rinsed with distilled water and the Tris–HCl 0.1 M buffer of pH 7.4 to remove unadsorbed HSA. The modified electrode was denoted as HSA–GCE throughout. It was now placed in buffer containing ferrocyanide as the redox probe and 120

consecutive potential cycles were applied with a scan rate of 50 mV $s^{-1}$. This procedure was repeated for 8 times to check the repeatability. We noticed that the peak currents of ferrocyanide changed by only 1.18% after 100 cycles which indicated that the HSA immobilization on the GCE surface is irreversible and uniform. This modified electrode was used to record the CV of NFR.

*Building an augmented matrix for MCR–ALS*

- *Experiment 1* (DPV experiment, $\mathbf{D}_{\mathbf{DPV}}^{\mathbf{NFR}}$): The concentration of NFR was kept constant (90.90 μM) and HSA was added to this solution in the range of 0.00–90.90 μM.
- *Experiment 2* (DPV experiment, $\mathbf{D}_{\mathbf{DPV}}^{\mathbf{HSA}}$): The concentration of HSA was kept constant (71.40 μM) and NFR was added to this solution in the range of 0.00–286 μM.
- *Experiment 3* (LSV experiment, $\mathbf{D}_{\mathbf{LSV}}^{\mathbf{NFR}}$): The applied procedure was the same as *Experiment 1*.
- *Experiment 4* (LSV experiment, $\mathbf{D}_{\mathbf{LSV}}^{\mathbf{HSA}}$): The applied procedure was the same as *Experiment 2*.
- *Experiment 5* (F experiment, $\mathbf{D}_{F}^{\mathbf{NFR},298}$): The concentration of NFR was kept constant (5 μM) and HSA was added to this solution in the range of 0.00–5 μM.
- *Experiment 6* (F experiment, $\mathbf{D}_{F}^{\mathbf{HSA},298}$): The concentration of HSA was kept constant (4.17 μM) and NFR was added to this solution in the range of 0.00–16.70 μM.
- *Experiment 7* (UVvis experiment, $D_{\mathbf{UVvis}}^{\mathbf{NFR}}$): The concentration of NFR was kept constant (5.00 μM) and HSA was added to this solution in the range of 0.00–5.00 μM.
- *Experiment 8* (UVvis experiment, $\mathbf{D}_{\mathbf{UVvis}}^{\mathbf{HSA}}$): The concentration of HSA was kept constant (5.00 μM) and NFR was added to this solution in the range of 0.00–20.00 μM.

To combine voltammetric and spectroscopic sub-matrices into an augmented matrix, all sub-matrices must contain the same number of rows and columns and must share the same distribution of the chemical species along the experiments. Ideally, this condition can be fulfilled using exactly the same total concentrations of NFR and HSA in all titrations, but this is not possible because the concentrations required for voltammetric experiments are higher than those for spectroscopic experiments. Thus, in the present work, voltammetric and spectroscopic experiments have been performed at different total concentrations but at the same values of ratio.

All of the performed experiments and their related data sets are described and coded in Table 1.

*Matrix augmentation and data treatment*

When a chemical system is monitored using more than one technique, e.g. DPV, LSV, F and UVvis a matrix is constructed, which consists of row- and column-wise augmented data [33]. The individual data matrices corresponding to the four types of technique are placed side-by-side. The related model for MCR–ALS analysis is shown below:

$$\begin{bmatrix} \mathbf{D}_{\mathbf{DPV}}^{\mathbf{NFR}} \mathbf{D}_{\mathbf{LSV}}^{\mathbf{NFR}} \mathbf{D}_{\mathbf{F}}^{\mathbf{NFR},298} \mathbf{D}_{\mathbf{UVvis}}^{\mathbf{NFR}} \\ \mathbf{D}_{\mathbf{DPV}}^{\mathbf{HSA}} \mathbf{D}_{\mathbf{LSV}}^{\mathbf{HSA}} \mathbf{D}_{\mathbf{F}}^{\mathbf{HSA},298} \mathbf{D}_{\mathbf{UVviz}}^{\mathbf{HSA}} \end{bmatrix} = \begin{bmatrix} \mathbf{C}^{\mathbf{NFR}} \\ \mathbf{C}^{\mathbf{HSA}} \end{bmatrix} \left[ \mathbf{S}_{\mathbf{DPV}}^{\mathbf{T}} \mathbf{S}_{\mathbf{LSV}}^{\mathbf{T}} \mathbf{S}_{\mathbf{F}}^{\mathbf{T}} \mathbf{S}_{\mathbf{UVvis}}^{\mathbf{T}} \right] + [\mathbf{E}_{\mathbf{DPV}} \mathbf{E}_{\mathbf{LSV}} \mathbf{E}_{\mathbf{F}} \mathbf{E}_{\mathbf{UVvis}}] \quad (5)$$

If $\mathbf{D_{DPV}}$, $\mathbf{D_{LSV}}$, $\mathbf{D_F}$ and $\mathbf{D_{UVvis}}$ are the measurements for four experiments obtained with the four techniques, there are two column-wise matrices of concentration profiles, $\mathbf{C^{NFR}}$ and $\mathbf{C^{HSA}}$ and four row-wise augmented matrices of measured profiles, $\mathbf{S}_{\mathbf{DPV}}^{\mathbf{T}}$, $\mathbf{S}_{\mathbf{LSV}}^{\mathbf{T}}$, $\mathbf{S}_{\mathbf{F}}^{\mathbf{T}}$ and $\mathbf{S}_{\mathbf{UVvis}}^{\mathbf{T}}$ which contain the pure signals for the techniques used to obtain $\mathbf{D_{DPV}}$, $\mathbf{D_{LSV}}$, $\mathbf{D_F}$ and $\mathbf{D_{UVvis}}$, respectively.

Solving Eq. (5) for $\begin{bmatrix} \mathbf{C}^{\mathbf{NFR}} \\ \mathbf{C}^{\mathbf{HSA}} \end{bmatrix}$ and $[\mathbf{S}_{\mathbf{DPV}}^{\mathbf{T}} \mathbf{S}_{\mathbf{LSV}}^{\mathbf{T}} \mathbf{S}_{\mathbf{F}}^{\mathbf{T}} \mathbf{S}_{\mathbf{UVvis}}^{\mathbf{T}}]$, facilitates the extraction of the related measured signals of all the species in the system.

However, the solutions to Eq. (1) obtained by MCR–ALS are not unique. They can have rotational and intensity ambiguities. To solve this limitation, column- and row-wise augmentation schemes (Eq. (5)) can be used for simultaneous resolution [33]. This kind of simultaneous data analysis is more powerful compared to that described by Eq. (1) and allows for improved resolution of very complex data structures. In general, this method should be useful to overcome some uncertainties in the analysis of the data related to coincidental processes or small signal shifts. Thus, in this work, an augmented matrix $\begin{bmatrix} \mathbf{D}_{\mathbf{DPV}}^{\mathbf{NFR}} \mathbf{D}_{\mathbf{LSV}}^{\mathbf{NFR}} \mathbf{D}_{\mathbf{F}}^{\mathbf{NFR},298} \mathbf{D}_{\mathbf{UVvis}}^{\mathbf{NFR}} \\ \mathbf{D}_{\mathbf{DPV}}^{\mathbf{HSA}} \mathbf{D}_{\mathbf{LSV}}^{\mathbf{HSA}} \mathbf{D}_{\mathbf{F}}^{\mathbf{HSA},298} \mathbf{D}_{\mathbf{UVviz}}^{\mathbf{HSA}} \end{bmatrix}$, was constructed and subsequently was used for next computations.

Because of the combination of completely different types of data, some considerations must be done in the analysis of the augmented matrix [20]:

(I) Due to the fact that voltammetry and spectroscopy are of very different magnitude, sub-matrices must be scaled in order to have a similar weight on the iterative ALS optimization of the augmented matrix; in a first approach, this is done by dividing all sub-matrices by its maximum value prior to their combination into an augmented matrix.

(II) The concept of component is a critical point. For spectroscopic data component is associated to pure chemical species in solution, but for electrochemical data component must be associated to a single electrochemical process giving a signal, including not only redox processes but also some other possible phenomena like, for instance, electrode adsorption of a species or capacitive currents due to the charging of the electrical double layer at the electrode surface. Anyway, in many situations, a single electrochemical process is produced by a single species. The number of components of each sub-matrix can be evaluated by SVD. Although this tool can be only considered as a guide since sometimes a component could be neglected if its concentration profile or its signal vector is a linear combination of others.

(III) In any iterative method, the application of appropriate constraints is crucial to drive the optimization to the right solution [34]. Below, the most generally used constraints in a process are described.

*Non-negativity* this constraint is the most used in resolution methods and prevents the presence of negative values in profiles.

*Unimodality* this constraint forces the only presence of one maximum in a species profile.

*Closure* this constraint is applied when the total concentration of all detectable species in each stage of a process is constant.

For more detailed explanation of the constraints the reader is referred to Ref. [34].

**Table 1**
Experiment coding used in this study.

| Data matrix | Species with constant concentration | Technique | Varying factor |
|---|---|---|---|
| $\mathbf{D}_{\mathbf{F}}^{\mathbf{HSA},298}$ | HSA | F | NFR |
| $\mathbf{D}_{\mathbf{F}}^{\mathbf{HSA},304}$ | HSA | F | NFR |
| $\mathbf{D}_{\mathbf{F}}^{\mathbf{HSA},310}$ | HSA | F | NFR |
| $\mathbf{D}_{\mathbf{F}}^{\mathbf{NFR},298}$ | NFR | F | HSA |
| $\mathbf{D}_{\mathbf{DPV}}^{\mathbf{NFR}}$ | NFR | DPV | HSA |
| $\mathbf{D}_{\mathbf{DPV}}^{\mathbf{HSA}}$ | HSA | DPV | NFR |
| $\mathbf{D}_{\mathbf{LSV}}^{\mathbf{NFR}}$ | NFR | LSV | HSA |
| $\mathbf{D}_{\mathbf{LSV}}^{\mathbf{HSA}}$ | HSA | LSV | NFR |
| $\mathbf{D}_{\mathbf{UVvis}}^{\mathbf{HSA}}$ | HSA | UVvis | NFR |
| $\mathbf{D}_{\mathbf{UVvis}}^{\mathbf{NFR}}$ | NFR | UVvis | HSA |

*Molecular dynamics simulations*

The crystal structure of HSA was downloaded from Brookhaven Protein Data Bank and the coordinates of chain A of the crystal structure were used to setup the system. All simulations were performed with the Gromacs package. The interaction parameters were computed by GROMOS96 force field. The water molecules were described by simple point charge (SPC) potential. The temperature was maintained at 300 K using the Berendsen thermostat. Pressure was maintained at 1 bar using semi-isotropic pressure coupling with the Parrinello-Rahman barostat. The coordinate of NFR was transferred into Gromacs topologies using the PRODRG2.5 server (beta). Then the complex was immersed in a cubic simulation box of extended SPC water molecules. The solvated system was neutralized by adding 16 sodium ions. The energy was minimized using steepest descent method. Production run employed the NPT (constant number of molecules, constant pressure, and constant temperature) ensemble. A cutoff value of 1.4 nm was used for computing van der Waals and Coulomb (short-range) forces, while the Particle Mesh Ewald (PME), was employed for computing the long range components of the electrostatic forces. Periodic boundary condition treatment for the box edge was employed and the neighbor list (with Cutoff 1.4 nm) updated after every 10 steps. Finally, the simulation was performed with a 2 fs time step.

## Results and discussion

*Fluorescence spectroscopic studies*

*Analysis of fluorescence quenching mechanism of HSA by NFR*

The fluorescence emission spectra of HSA in the presence of different added amounts of NFR at three temperatures (i.e., 298, 304 and 310 K) were recorded and one of them (298 K) is shown in Fig. 1(A). It is observed a gradual decrease in the initial HSA fluorescence emission without changes in the wavelength of maximum emission.

Fluorescence quenching refers to any process that decreases the fluorescence intensity of a sample. A variety of molecular interactions can result in quenching, such as excited state reactions, molecular rearrangements, energy transfer, ground state complex formation, and collisional quenching [30]. The mechanisms of quenching are usually classified as either dynamic (collisional encountering between the fluorophore and quencher) or static (formation of a non-fluorescent ground state complex) [30]. Fluorescence quenching is described by the well-known Stern–Volmer equation:

$$\frac{F_0}{F} = 1 + K_{SV}[Q] = 1 + k_q\tau_0[Q] \quad (6)$$

where $F_0$ and $F$ are the fluorescence intensities in the absence and presence of the quencher (NFR), respectively, $K_{SV}$ is the Stern–Volmer quenching constant, [Q] is the concentration of the quencher, $\tau_0$ is the average lifetime of molecule without quencher and$k_q$is the quenching rate constant of bimolecule. Therefore, Eq. (6) was applied to determine $K_{SV}$ by linear regression of a plot of $F_0/F$ versus[Q]. The possible quenching mechanism can be interpreted by following the changes in$K_{SV}$as a function of temperature [30]. The Stern–Volmer plots for quenching the fluorescence emission of HSA by NFR at three temperatures are shown in Fig. 1(C) and the estimated parameters of Eq. (6) are listed in Table 2. The results reveal that the Stern–Volmer quenching constant $K_{SV}$ is inversely correlated with temperature which confirms that the probable quenching mechanism of fluorescence of HSA by NFR is coming from complex formation (Static quenching).

The value of $k_q$ also gives information about the mechanism of quenching. It is well-known that the maximum scatter collision quenching constant of various quenchers with a biopolymer is

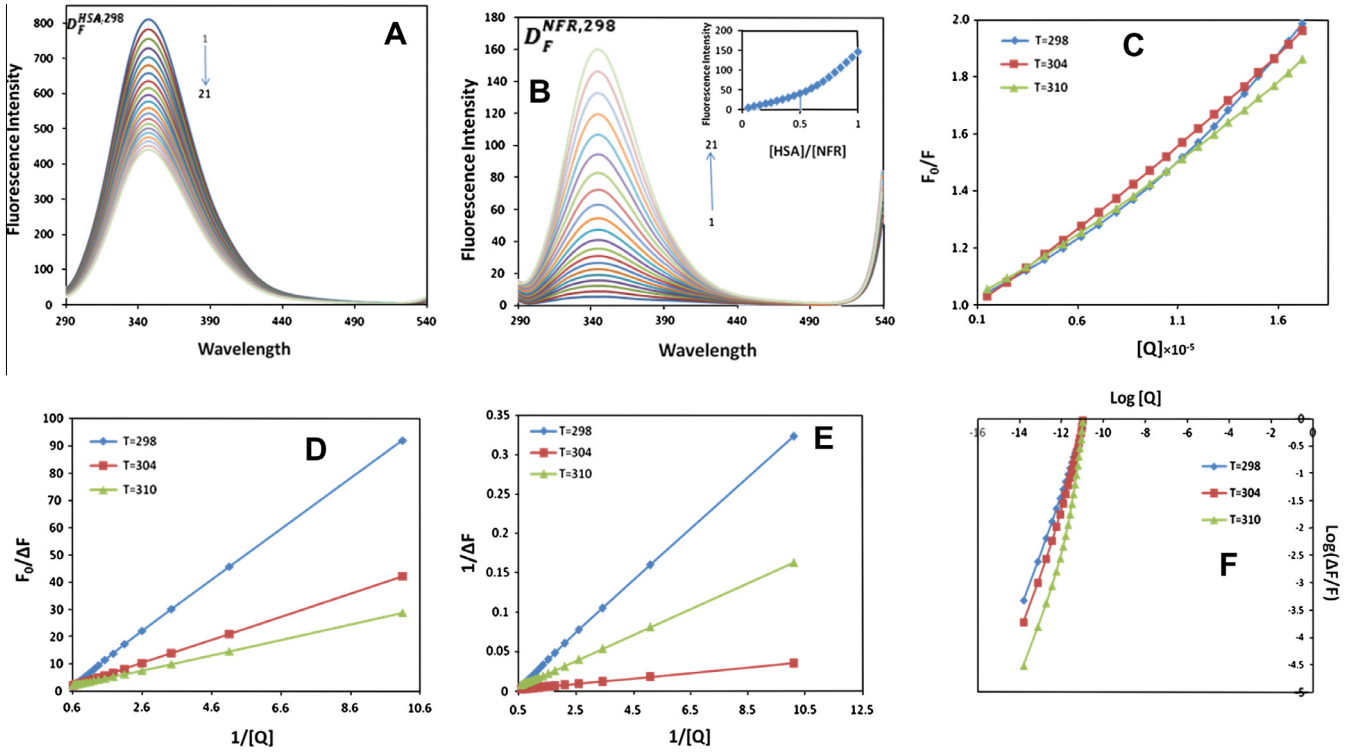


**Fig. 1.** (A) Fluorescence spectra of HSA in the presence of increasing concentration of NFR at 298 K. Concentration of HSA was constant at 4.17 μM and NFR was added in the range of 0.00–16.70 μM. (B) Fluorescence spectra of NFR in the presence of increasing concentration of HSA at 298 K. Concentration of NFR was constant at 0.47 μM and HSA was added in the range of 0.00–0.47 μM. Inset: mole-ratio plot. (C) The Stern–Volmer, (D) the modified Stern–Volmer, (E) the Lineweaver–Burk and (F) double-log plots for quenching HSA with NFR at three different temperatures.

$1.0 \times 10^{10}$ L mol$^{-1}$ s$^{-1}$ [30]. To calculate $k_q$, we need the value of $\tau_0$, which for a biomacromolecule it is assumed to be $10^{-8}$ s [35]. As it is obvious from Table 2, the quenching constants of HSA by NFR, calculated at different temperatures, are larger than the suggested threshold value for scatter collision, which is another indication of the static quenching. Since the quenching mechanism is most probably proceeding by complex formation (static quenching), the quenching process was further analyzed according to the modified Stern–Volmer equation [30]:

$$\frac{F_0}{\Delta F} = \frac{F_0}{F_0 - F} = \frac{1}{f_a k_a}\frac{1}{[Q]} + \frac{1}{f_a} \tag{7}$$

where $\Delta F$ is the difference in fluorescence intensity in the presence ($F$) of the quencher at concentration [$Q$] and in the absence ($F_0$) of quencher. The parameter $k_a$ is the effective quenching constant for the accessible fluorophores, which is analogous to the associative binding constants for the quencher–acceptor system [36], and $f_a$ is the fraction of accessible fluorescence. As it is observed from Fig. 1(D), the dependence of $F_0/\Delta F$ on the reciprocal value of the quencher concentration 1/[Q] is linear at all studied temperatures. The estimated fitting parameters are shown in Table 2. The decreasing trend of $k_a$ with increasing temperature is in accordance with $K_{SV}$'s dependence on temperature as mentioned above.

The quenching data was also analyzed by the Lineweaver–Burk equation [37] as follows:

$$\frac{1}{F_0 - F} = \frac{1}{F_0} + \frac{1}{k_{LB} F_0 [Q]} \tag{8}$$

where $k_{LB}$ is the static quenching constant that describes the efficiency of quenching at the ground state and could be obtained from the ratio of the intercept to slope of the Lineweaver–Burk plot (See Fig. 1(E)). The results are presented in Table 2. These values are in good agreement with the $K_{SV}$ values and also with the $k_a$ values.

*Calculation of binding constant and binding capacity*

After confirming the quenching as static, the binding constant values were determined from the following equation [38]:

$$\log\frac{F_0 - F}{F} = \log K_b + n \log[Q] \tag{9}$$

where $K_b$ is the binding constant andnis the number of binding sites per protein. The linear plots, Fig. 1(F), of log ($F_0 - F/F$) versus log[Q] for NFR binding to HSA gave $K_b$ andnvalues those are presented in Table 2. This indicated the formation of a 2:1 complex of NFR–HSA. These results together with the estimated effective quenching constants suggest that the binding constant between NFR and HSA is high and hence NFR can be stored and carried by this protein in the body.

*Interaction forces*

The interaction forces between a small molecule and a biomacromolecule include four types of interactions, namely hydrogen bonding, van der Waals interactions, electrostatic forces and hydrophobic interactions [39]. In order to explore the interaction of NFR with HSA, the thermodynamic parameters were calculated from the van't Hoff equation and corresponding thermodynamical functions based on the temperature effect.

$$\ln K = -\frac{\Delta H}{RT} + \frac{\Delta S}{R} \tag{10}$$

$$\Delta G = -RT \ln K = \Delta H - T\Delta S \tag{11}$$

where $K$ is analogous to $K_a$ at the corresponding temperature, $R$ is the gas constant, and $\Delta H$, $\Delta G$ and $\Delta S$ are enthalpy change, Gibbs free energy change and entropy change, respectively. From the thermodynamic standpoint, $\Delta H > 0$ and $\Delta S > 0$ implies a hydrophobic interaction, $\Delta H < 0$ and $\Delta S < 0$ reflects the van der Waals force or hydrogen bond formation and $\Delta H < 0$ and $\Delta S > 0$ suggesting an electrostatic force [40].

From the equations above, the thermodynamic functions involved in the binding process were calculated and reported in Table 2. The negative sign for $\Delta G$ means that the binding process is spontaneous. The negative values of $\Delta H$ and $\Delta S$ indicate that the binding is mainly enthalpy driven, whereas the entropy is unfavorable for it and also reveal that the binding process investigated here is mainly driven by van der Waals force or hydrogen bonding.

*Site selectivity of binding of NFR to HSA*

To a mixture of[NFR]/[HSA], the site marker (Wr or Ip) was added in the range of 0.00–16.00 μM. The percentage of the initial fluorescence due to the fluorescent probe was calculated as: $(F_2/F)_1 \times 100$ (Section 'Site selectivity of binding NFR to HSA') and plotted versus [Site marker]/[HSA] (Fig. S2). The changes induced by the site markers were used to interpret the site selectivity of binding of NFR to HSA. The obtained results showed that by the addition of Wr to the solution of HSA-NFR, the fluorescence intensity of the HSA decreased gradually and this suggests an increase in the polarity of the region surrounding the tryptophan site (Trp214), and indicating that the binding of NFR to HSA was affected by addition of Wr. In contrast to Wr, the fluorescence intensity of HSA in presence of Ip was almost the same as in the absence of Ip (see Fig. S2 for comparison), indicating that Ip did not prevent the usual binding location of NFR on HSA. The obtained results showed that Wr competed with NFR molecules while Ip did not. Hence the fluorescence of the complex was affected in presence of Wr while with Ip it remained invariant. Therefore, we inferred that the binding site of NFR was mainly located in hydrophobic pocket in sub-domain IIA of HSA.

*The UVvis absorption studies*

In order to explore the structural change in HSA and to confirm the complex formation between NFR and HSA, the UVvis absorption measurements were made. The UVvis absorption studies were carried out by keeping the NFR concentration constant and increasing the concentration of HSA (Fig. 2(A)). The NFR exhibited a maximum absorption at 277 nm and its intensity was increased gradually upon the addition of HSA (Fig. 2(A)). Moreover, a new peak at 212 nm is forming gradually upon the addition of HSA which may be related to complex formation. According to the mole-ratio plot (inset of Fig. 2(A)) two inflection points at [HSA]/

**Table 2**
Estimated parameters by the use of different equations reported in this study.

| $T$ (K) | $10^{-4}$ $K_{SV}$($M^{-1}$) | $10^{-12}$ $K_q$ ($M^{-1}$ $S^{-1}$) | $R^2$ | $10^{-4}$ $K_a$ | $R^2$ | $K_{LB}$ | $R^2$ | $10^{-5}$ $K_b$ ($M^{-1}$) | $n$ | $R^2$ | $\Delta H$ (kJ mol$^{-1}$) | $\Delta S$ (J mol$^{-1}$ K$^{-1}$) | $\Delta G$ (kJ mol$^{-1}$) |
|---|---|---|---|---|---|---|---|---|---|---|---|---|---|
| 298 | 5.9805 | 5.9805 | 0.9823 | 3.5995 | 0.9995 | 4.2000 | 0.9995 | 6.4201 | 1.85 | 0.9992 | −87.03 | −204.73 | −26.02 |
| 304 | 5.9440 | 5.9440 | 0.9978 | 1.5590 | 0.9999 | 1.6667 | 0.9998 | 7.3651 | 1.88 | 0.9528 | | | −24.79 |
| 310 | 5.1568 | 5.1568 | 0.9962 | 1.3763 | 0.9998 | 1.2000 | 0.9999 | 8.1461 | 1.93 | 0.9911 | | | −23.56 |

[NFR] ~0.5 and [HSA]/[NFR] ~1 were observed which confirmed formation of two 2:1 and 1:1 NFR–HSA complex species, respectively. On the other hand, when the UVvis absorption experiments were carried out on a solution containing HSA with a constant concentration, three absorption peaks at 206, 222 and 280 nm were observed (Fig. 2(B)). The intensities of these peaks were changed (the insets of Fig. 2(B)) upon the addition of NFR. The peak at 280 nm would found to be shifted to 3 nm towards higher wavelengths in the presence of increased amounts of NFR. These changes in $\lambda_{max}$ indicated the change in polarity around the tryptophan residue of HSA and hence the change in hydrophobicity. According to these results, we proposed that the binding between NFR and HSA led to changes in HSA conformation. Moreover, as can be seen from the top inset of Fig. 2(B) three isosbestic points were produced upon the addition of NFR. These three isosbestic points may be related to the co-existence of four species in the solution. According to the obtained results we think these four species may be free NFR, free HSA, and two complex species. Therefore, the system would be further analyzed by MCR–ALS as a powerful chemometric tool in next sections to make a strong decision about the species.

*Energy transfer to NFR and the binding distance measurement*

Fluorescence energy transfer (FRET) has been used as a 'spectroscopic ruler' for measuring molecular distance in biological systems [41]. The FRET efficiency depends on the extent of overlap of the donor emission and acceptor absorption, orientation of the transition dipole of the donor and the distance between the donor and acceptor which must be within the Forster distance of 2–8 nm [42]. The efficiency ($E$) of FRET process depends on the inverse sixth power of the distance between donor and acceptor ($r$) and of the critical energy transfer distance or Forster radius ($R_0$). When the efficiency of transfer is 50%, a condition of 1:1 situation of donor to acceptor concentration prevails and $E$ is expressed by the equation:

$$E = 1 - \frac{F}{F_0} = \frac{R_0^6}{(R_0^6 + r^6)} \tag{12}$$

$R_0$ can be calculated using the following relation:

$$R_0^6 = 8.8 \times 10^{-25} k^2 n^{-4} \Phi J \tag{13}$$

where $k^2$ is the spatial factor of orientation, $n$ is the refractive index of the medium and $\Phi$ is the fluorescence quantum yield of the donor. The $J$ is the overlap integral of the fluorescence emission spectrum for the donor and the absorption spectrum of the acceptor (Fig. 3) which may be calculated from the equation given below:

$$J = \frac{\int_0^\infty F(\lambda)\varepsilon(\lambda)\lambda^4 d\lambda}{\int_0^\infty F(\lambda) d\lambda} \tag{14}$$

where $F(\lambda)$ and $\varepsilon(\lambda)$ is the fluorescence intensity of the donor and molar absorption coefficient of the acceptor, respectively at the wavelength $\lambda$. Using the values of $k^2 = 2/3$, $n = 1.336$, and $\Phi = 0.118$ [43], the values of $J$, $R_0$, $E$ and $r$ have been calculated to be $1.87 \times 10^{-14}$ cm$^3$ M$^{-1}$, 4.06 nm, 0.034 and 7.09 nm, respectively. The donor to acceptor distance is less than 8 nm and $0.5R_0 < r < 2.0R_0$ which indicate that the energy transfer from HSA to NFR occurs with high probability.

*Voltammetric studies*

*Cyclic voltammetric measurements*

The electrochemical behavior of NFR at the GCE was studied by cyclic voltammetry. The CV of NFR at the GCE in Tris–HCl buffer with pH = 7.4 was commenced at 0.00 V and its direction was reversed at 0.80 V. The results (Fig. 4, Curve 1) showed a well-defined anodic peak at 340 mV and a weaker counterpart cathodic peak at 221 mV that may be due to adsorption of NFR at the surface of GCE. The insets (A and B) of Fig. 4 show the effects of $\upsilon$ and $\upsilon^{1/2}$ on the CV response of NFR, respectively. The anodic peak increased linearly with $\upsilon$ (the inset (A) of Fig. 4), indicating a surface-controlled electrochemical reaction.

Furthermore, the pH dependence behavior of NFR was investigated in Tris–HCl buffer solutions at various pHs (2.00–12.00) and the results are summarized in Fig. S3. As can be seen a nearly well defend anodic and cathodic peaks are observable at pH = 2 which their peaks potential were shifted toward less positive values by increasing the pH of the solution. At pHs higher than 8 no significant anodic and cathodic peaks were observed. These results showed that the electrodic process is pH dependent. The negative shift in the anodic peak potential with pH showed a linear behavior with a slope of 0.0395 V per unit pH and a $R^2$ of 0.9909 (the inset of Fig. S3). Based on the following equation we can obtain m/$n$ ~ 0.5.

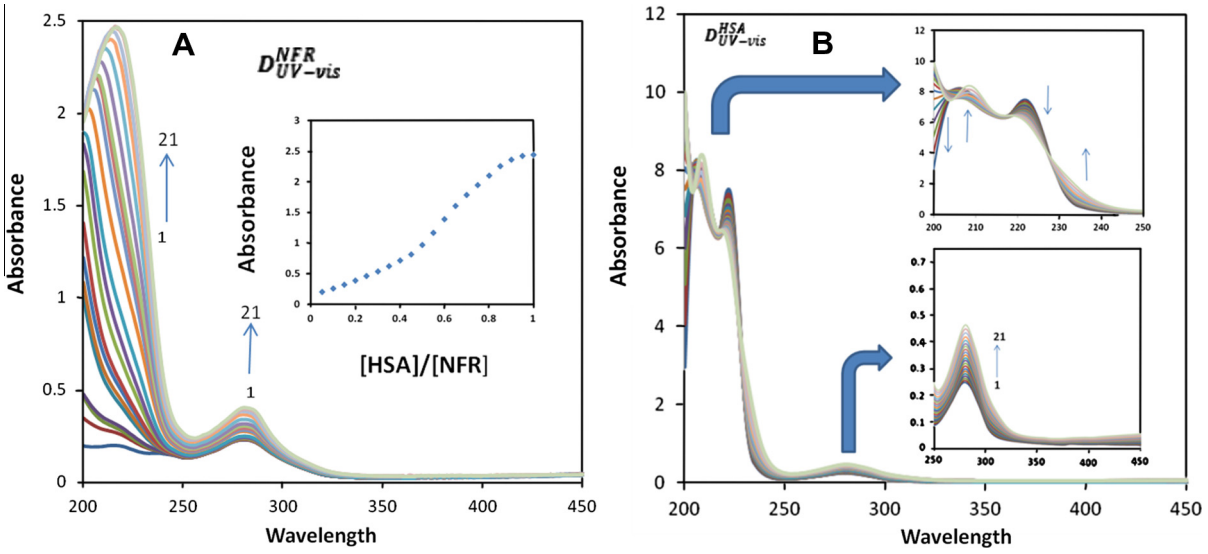


**Fig. 2.** The UVvis absorption spectra of (A) NFR (5.00 μM) in the presence of increasing concentration of HSA (0.00–5.00 μM), inset: mole-ratio plot, and (B) HSA (5.00 μM) in the presence of increasing concentration of NFR (0.00–20.00 μM).

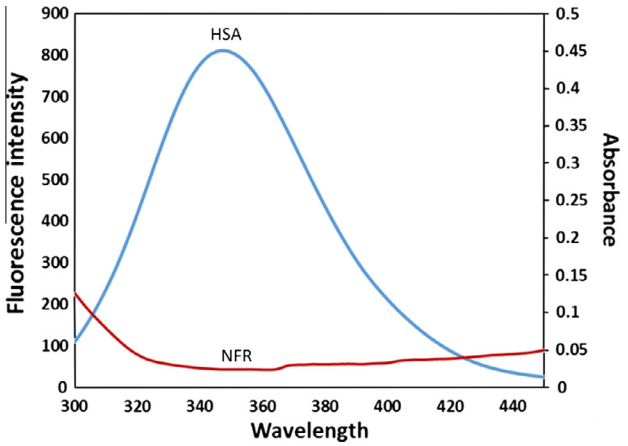


**Fig. 3.** Overlay of fluorescence emission spectrum of HSA and UVvis absorption spectrum of NFR at pH 7.40 and $T = 298$ K.

$$E_{\frac{1}{2}} = E^{0\prime} - \left(\frac{59}{n}\right) \text{mpH} \quad (15)$$

where $m$ and $n$ are the number of proton and electron involved in redox process, respectively.Scheme 1 shows the probable mechanism for oxidation of NFR at the GCE.

The CVs of NFR at the GCE in the presence of increasing HSA concentration are shown in Fig. 4. The drop in peak current of NFR was significant up to 30 s. After 30 s, the peak current remained constant. Therefore, the interaction time of 30 s was maintained for each measurement upon the addition of HSA. Significant decrease in peak current and positive shift in anodic peak potential of NFR was observed upon the addition of HSA. As can be seen from the mole-ratio plot (the inset (C) of Fig. 4) formation of a 2:1 NFR–HSA complex was confirmed.

The equilibrium concentration of free NFR decreased in the presence of HSA as evident from the decrease in peak current. It has been observed that when an interaction of some biopolymers such as hemoglobin, SA and DNA with small molecules takes place at quite a low biopolymer concentration and a short accumulation time, only about 10% of the electrode surface may be covered; this implies that very little competitive adsorption of small molecules can occur. Hence, we proposed that the NFR embedded within the HSA structure, which results in the decrease of its equilibrium concentration in solution. However, there is another possible explanation for these observations, and it involves the possible unfolding of the HSA structure as the concentration of the NFR increases. As a result, the protein structure unravels, and this provides pathways for the NFR to access the tryptophan or tyrosine residues, which then can be oxidized at the GCE.

The immobilization of HSA onto an electrode surface is in many ways the crucial aspect of the developing HSA biosensors for monitoring ligand since it dictates the accessibility of HSA to ligand in solution and hence can influence the affinity of ligand binding. In view of this, we also carried out the interaction studies at the HSA–GCE which was prepared by immobilization technique. The electrochemical behavior of NFR at the HSA–GCE was compared with that obtained at the GCE. The CV of NFR showed an oxidation peak at 340 mV and a reduction peak at 221 mV with bare GCE. The oxidation peak was found to be shifted towards more positive potential (387 mV) and reduction peak was noticed at 275 mV with HSA–GCE (Fig. S4). This shift in peak potential could be related to the presence of HSA at the electrode surface and the interaction between NFR and HSA. Heli et al. [44] have attributed the observed shifts at the HSA–GCE to hydrophobic interactions. The observed shifts in peak potentials in this study indicated that the interaction

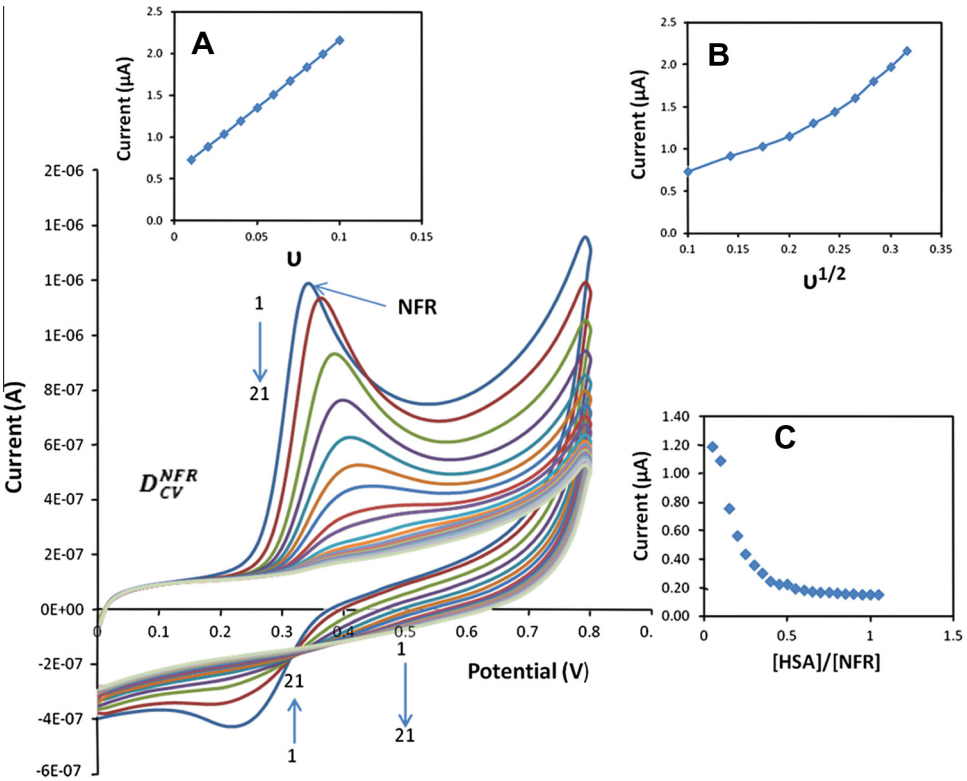


**Fig. 4.** The CVs of NFR (90.90 μM) with different concentrations of HSA (0.00–90.90 μM) at the GCE. Inset (A): variation of $i_{pa}$ versus $\upsilon$ (V), Inset (B): variation of $i_{pa}$ versus $\upsilon^{1/2}$ (V), Inset (C): the mole-ratio plot.

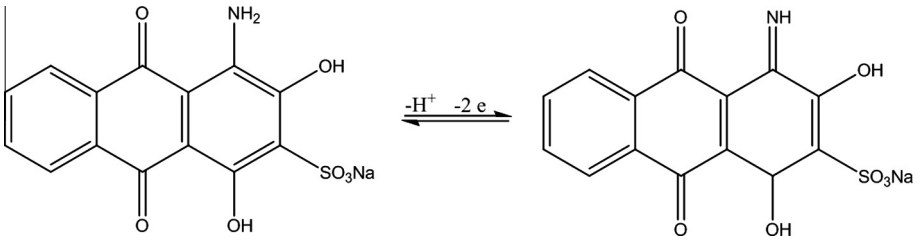


**Scheme 1.** The proposed mechanism for oxidation of NFR at the GCE.

of NFR with HSA occurred through hydrophobic interaction. This result is a golden result to confirm the binding site of NFR was mainly located in hydrophobic pocket in sub-domains IIA of HSA and also is a guarantee which confirms the results of spectroscopic methods.

*The Linear sweep and differential pulse voltammetric studies*

The LSVs of NFR in a Tris–HCl (pH 7.4) buffer solution collected at the GCE indicated that the anodic peak current decreased continually and the peak potential shifted to more positive values upon the addition of HSA (Fig. 5(A)). From the mole-ratio plot (the inset of Fig. 5(A)) formation of a 2:1 NFR–HSA complex was confirmed.

Typical LSVs of HSA in the presence of increasing concentration of NFR (Fig. 5(B)) not only revealed that HSA is electro-inactive at the GCE but also revealed that there was not any observable peak until [NFR]/[HSA] ~1. After this ration the peak current increased with increasing concentration of NFR. With these observations, there was little strong evidence to suggest the formation of a NFR–HSA complex, and consequently, it may be concluded that the increase in peak current is due mostly to the presence of free NFR. Another possible explanation could be that the nature of the structural changes induced in HSA during its interaction with NFR resulted in the unfolding or denaturation of the protein; this facilitated easy access to the tryptophan and tyrosine residues for oxidation (Complex formation). The oxidation peak of the free NFR and that of the tryptophan/tyrosine residues of NFR–HSA complex overlap, and the recorded profile was the sum of these two phenomena, which increased together with the addition of NFR.

The results of DPV experiments at the GCE are shown in Fig. 5(C and D). The observed variations are the same as LSV measurements which need the same justifications. Therefore, we think repeating them is redundant.

The most important results of voltammetric experiments are represented in mole-ratio plots (Fig. 5(E and F) and the insets of

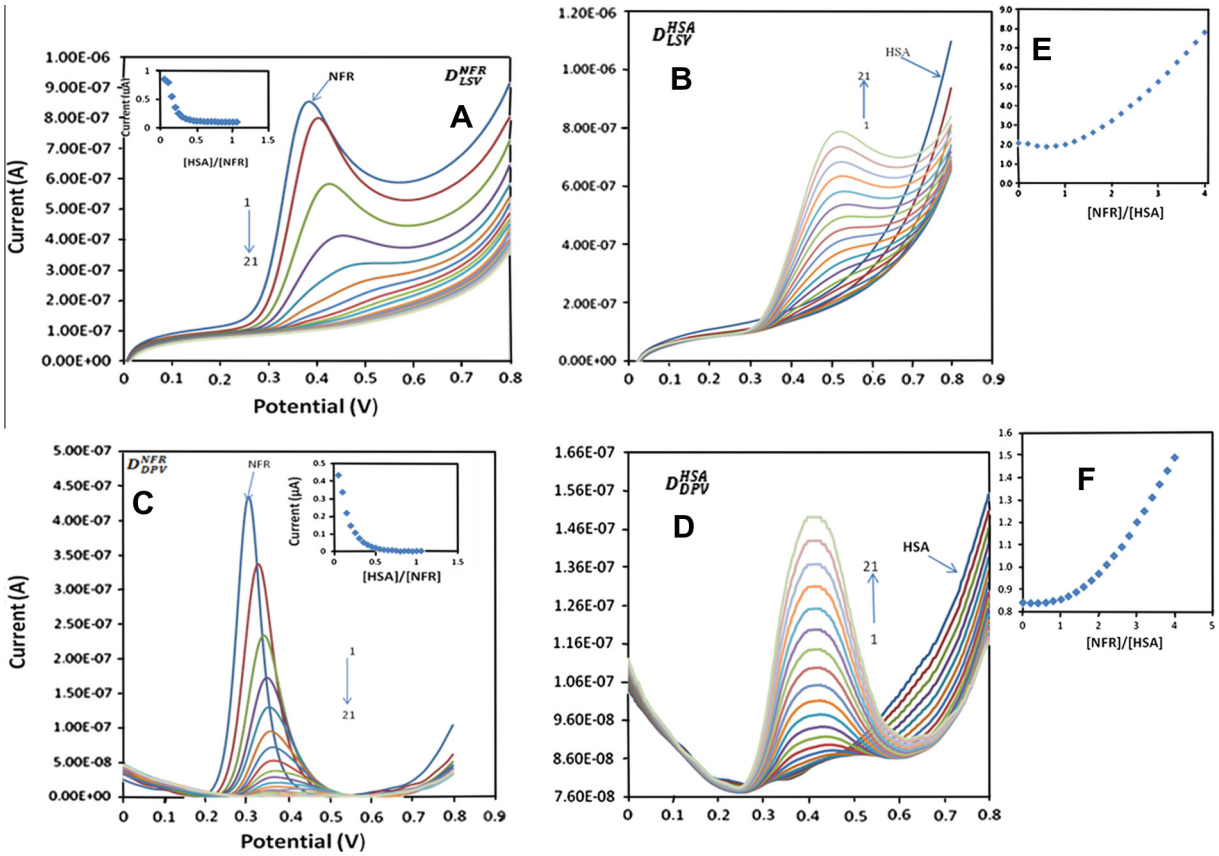


**Fig. 5.** The results of voltammetric experiments. LSV: (A and B), and DPV: (C and D). (E and F) are mole-ratio plots. For knowing the concentrations of these experiments see Section 'Building an augmented matrix for MCR–ALS'.

Fig. 5(A and C)). As can be seen from these plots formation of two 1:1 and 2:1 NFR–HSA complex species may be concluded which confirm the UVvis results.

Further interpretation of the NFR–HSA interaction on the basis of direct observations of the measured profiles was difficult because the recorded data especially the F data (Fig. 1(A and B)) was suffered from rank deficiency. Therefore, multivariate analysis was applied to extract further information.

*Combined spectroscopic and voltammetric studies*

The augmented matrix described at Section 'Matrix augmentation and data treatment' was submitted for the simultaneous resolution by the MCR–ALS. Before starting the resolution, the number of contributions to the augmented matrix was determined by SVD and here, the SVD detected four components. These four components may be related to free NFR, free HSA and two complex species. Taking into account that MCR–ALS needs information as real as possible to start the resolution, the *C* matrix was estimated by the use of the EFA.

Below, the used constraints in the iterative ALS optimization are described.

*Non-negativity* this constraint is the most used in resolution methods and prevents the presence of negative values in profiles. It was applied to both concentration and signal profiles because their values are always positive.

*Unimodality*: it was applied to signal profiles.

*Closure*: applying a closure constraint to the matrices obtained at different concentration levels is impossible.

By applying the mentioned constraints, the ALS optimization was started. As previously mentioned, the lof which is defined as the difference between the input data, *D*, and the data reproduced from the $CS^T$ product obtained by MCR–ALS, was used as a parameter to evaluate the goodness of fit of the model. In this work, the best lof value was found to be 6.64% which implies that almost all of the variability in the experimental data presented as a product of the extracted signals and the concentration profiles, is explained. Standard deviation of the residuals was also found to be 0.015.

The results of MCR–ALS are shown in Fig. 6(A–F). The Fig. 6(A) showed that the concentration of NFR (black line) is decreasing and two new species (the first one: yellow line and the second one: red line) are forming upon the addition of HSA.

The concentration of the first species increased sharply and reached a maximum at [HSA]/[NFR] ~0.15 while formation of the second species is started after this point of titration. As can be seen from Fig. 6(A), the concentration of the second species increased and reached equilibration at [HSA]/[NFR] ~1. It can be concluded that the second species is a 1:1 NFR–HSA complex species. As can be seen from Fig. 6(A), the HSA (green line) is released nearing the end of titration. It can help us to know that the complex formation is finishing and only two complex species were formed upon the addition of HSA to NFR. According to the described observations, judgment about the stoichiometry of the first complex species is difficult therefore, to make a reasonable decision about this species we have to consider the results of Fig. 6(B) as well. This figure showed that the concentration of the second species increased and reached a maximum at [NFR]/[HSA] ~1.2 which confirms

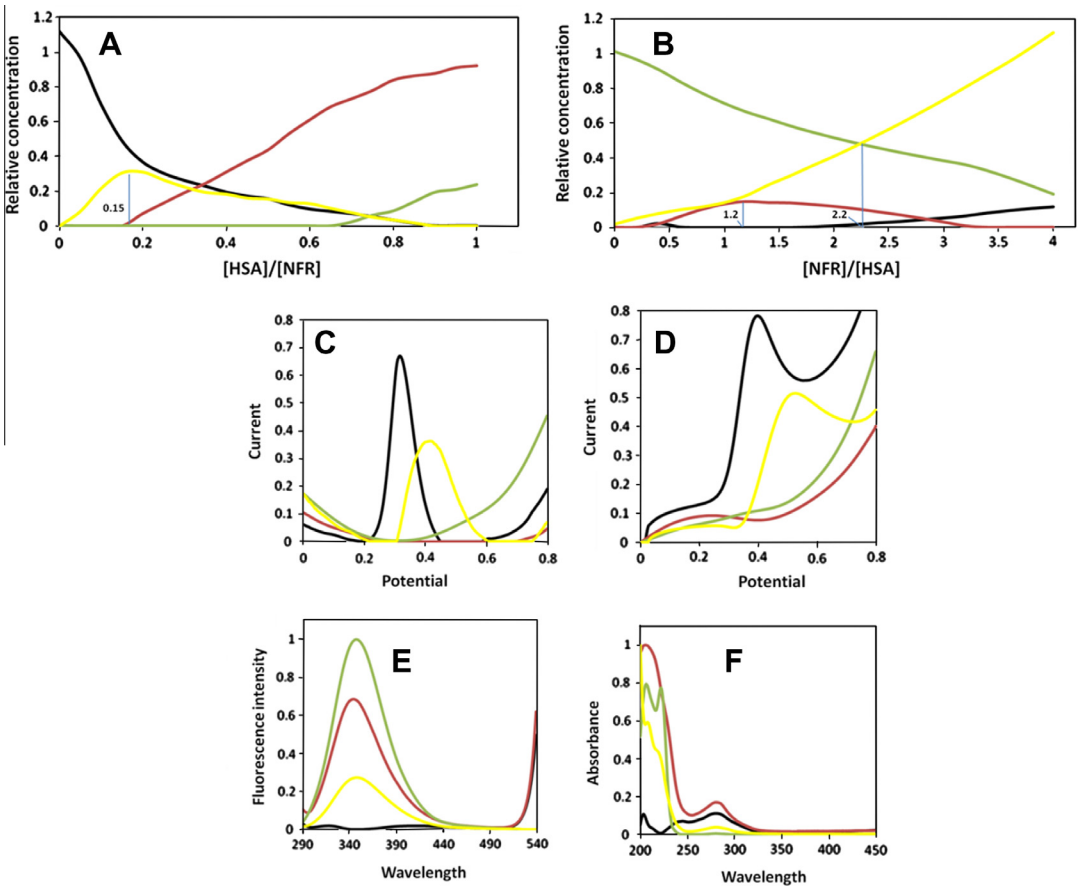


**Fig. 6.** The results of MCR–ALS: (A and B) Extracted concentration profiles. (C–F) Extracted signal profiles of different species involved in DPV, LSV, F and UVvis experiments, respectively. NFR: black line, HSA: green line, 1:1 NFR–HSA complex species: red line and 2:1 NFR–HSA complex species: yellow line. (For interpretation of the references to color in this figure legend, the reader is referred to the web version of this article.)

**Table 3**
Results of applying EQUISPEC.

| Analyzed matrix | $K_b$ | |
|---|---|---|
| | $^{*}PL_2$ | PL |
| $\left[D^{NFR}_{DPV} D^{NFR}_{LSV} D^{NFR,298}_{F} D^{NFR}_{UVvis}\right]$ | $7.01 \times 10^5$ | $11.33 \times 10^3$ |
| $\left[D^{HSA}_{DPV} D^{HSA}_{LSV} D^{HSA,298}_{F} D^{HSA}_{UVvis}\right]$ | $7.11 \times 10^5$ | $11.48 \times 10^3$ |
| $\left[\begin{matrix} D^{NFR}_{DPV} D^{NFR}_{LSV} D^{NFR,298}_{F} D^{NFR}_{UVvis} \\ D^{HSA}_{DPV} D^{HSA}_{LSV} D^{HSA,298}_{F} D^{HSA}_{UVvis} \end{matrix}\right]$ | $7.5 \times 10^5$ | $12.08 \times 10^3$ |

P: HSA, and L: NFR.

formation of a 1:1 NFR–HSA complex. But by casting a wary eye on this figure, it can be observed that the NFR is releasing at [NFR]/[HSA] ~2.2 and this means that the complex formation is finishing. Prior to this point of titration the whole of added NFR was consumed by complex formation. Therefore, by these observations we can conclude that the unknown species is a 2:1 NFR–HSA complex.

The obtained signal profiles by MCR–ALS for four types of data are shown in Fig. 6(C–F). From these figures the valuable information about the nature of the involved complex species in each technique could be obtained. According to these results, it is clear that the 1:1 NFR–HSA complex species is electro-inactive while the 2:1 NFR–HSA complex species is electroactive at the GCE. The extracted HSA profile suggested that the protein in its original structural format is electro-inactive.

According to the results obtained by MCR–ALS and regarding the obtained results from the previous sections, it can be found that voltammetric and UVvis methods were successful to obtain the number and also the stoichiometries of the complex species, but the F data was suffered from rank deficiency therefore, only one complex species was found from their results. The rank deficiency observed in F data was broken by matrix augmentation as powerful chemometric strategy.

### *Hard-modeling approach*

In the case of hard-modeling approaches, a model is applied to guide the decomposition of matrix *D* following Eq. (1). As an example, in the case of protein–ligand interaction, the model includes the stoichiometry of the species formed, as well as initial trial value for the binding constant. This value is used to build an initial estimation of the concentration profiles included in *C*. Once this estimation is obtained, a least squares fit is performed to obtain the pure spectra in $\mathbf{S^T}$ that best match the concentration profiles in *C* and the data in *D*. A residual matrix *E* is then calculated from the difference between the data in *D* and the reproduced data matrix. The optimization procedure continues by tuning the stoichiometry of the proposed species until a desired level of residuals *E* is reached. A more detailed explanation of the mathematical basis of the algorithms used in these calculations can be found in Dyson et al. [45].

EQUISPEC, a hard-modeling algorithm, was applied to an augmented matrix (combined spectroscopic and voltammetric data) to compute the binding constants and also verify the results of Section 'Calculation of binding constant and binding capacity'. The results of this study are shown in Table 3. As can be seen, there is a good agreement between the binding constant values computed by EQUISPEC and also with the results reported at Section 'Calculation of binding constant and binding capacity'.

### *Molecular modeling studies*

#### *Molecular docking*

In this study, the Arguslab program was used to realize the binding mode of NFR at the active site of HSA. The main aspect

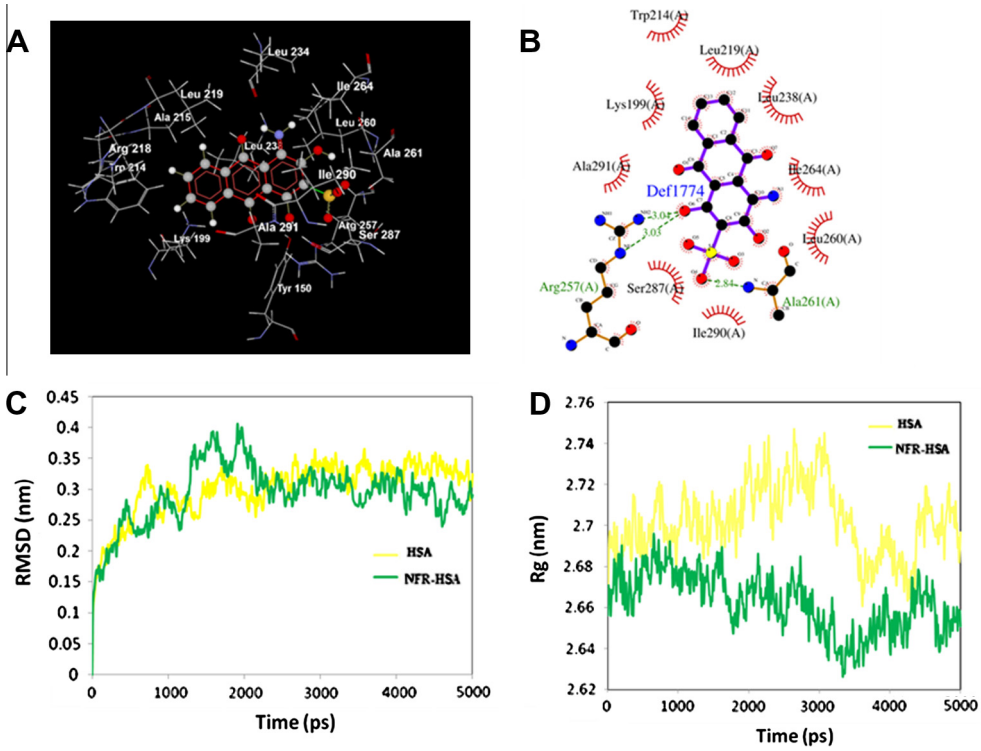


**Fig. 7.** (A) The NFR docked in the binding pocket of HSA. The hydrophobic residues of HSA are represented using lines and the NFR is represented using ball and stick model. (B) The computer-generated model of interaction of NFR with HSA by LIGPLOT. (C and D) The results of MD simulations, (C) time dependence of rmsd's. (D) Time evolution of the radius of gyration (Rg).

for the ligand docking postures was considering the effective interaction of NFR with the various amino acid residues in the active site. The binding sites were obtained as Leu234, Leu219, Ala215, Arg218, Trp214, Lys199, Ala291, Tyr150, Leu238, Ile290, Arg257, Ser287, Ala261, Leu260 and Ile264 (See Fig. 7(A)). The$\Delta$ Gfor the binding of NFR to HSA was $-27.14\ kJ\ mol^{-1}$. This result is very close to that obtained by experimental methods (Table 2).

The docking results showed that NFR binds within the binding pocket of sub-domain IIA. The binding site of the HSA was studied to understand the nature of the residues defining the site. The LIGPLOT program was used to explore the hydrogen bonds interactions between HSA and NFR as shown in Fig. 7(B). Three hydrogen bonding interactions were observed.

*Analysis of the dynamics trajectories*

The MD simulations were performed on HSA and NFR–HSA complex to investigate the dynamics properties of protein and complex in water by means of root mean square deviations (rmsd's) of protein and complex with respect to the initial structure and the radius of gyration (Rg) of protein. The rmsd and Rg values of atoms in HSA and NFR–HSA complex were plotted from 0 to 5000 ps as shown in Fig. 7(C and D), respectively. Analysis of the Fig. 7(C) indicated that the rmsd of both systems reaches equilibration and oscillates around an average value after 3000 ps simulation time. The rmsd values of atoms in HSA and NFR–HSA complex were calculated from a 3000–5000 ps trajectory, where the data points were fluctuated for HSA ($0.330 \pm 0.014$ nm) and NFR–HSA complex ($0.295 \pm 0.020$ nm). Moreover, radius of gyration (Rg) of HSA and NFR–HSA complex is a measure of its compactness. Then, we determined the Rg values of HSA and NFR–HSA complex as shown in Fig. 7(D). In both systems, Rg values were stabilized at about 3300 ps. Initially, the Rg value of both HSA and NFR–HSA complex was about 2.650 nm. The HSA and NFR–HSA complex were stabilized at $2.697 \pm 0.010$ and $2.675 \pm 0.008$ nm, respectively. These results indicated that the Rg value is not compatible upon NFR complexation with respect to free HSA. Therefore, it may be concluded that the structure of the HSA in the presence of NFR is unfolded during MD simulation.

## Conclusion

This paper demonstrates a detailed investigation on the interaction between NFR and HSA using experimental and computational approaches which has been reported for the first time. The fluorescence spectroscopic data showed that the NFR could insert into the HSA and quenches its intrinsic fluorescence by static mechanism. The UVvis absorption measurements showed that the binding between NFR and HSA led to changes in the HSA conformation. Based on the electrochemical data, the hydrophobic mode of interaction between NFR and HSA was proved. New information resulted, when the augmented matrix was resolved by the MCR–ALS. The extracted concentration profiles indicated formation of two 1:1 and 2:1 NFR–HSA complex species which were electro-inactive and electroactive, respectively. The F data was suffered from rank deficiency but it was broken by matrix augmentation as powerful chemometric strategy. The independent molecular modeling studies resulted in binding mechanism very close to the experimental one. Both experimental and computational studies proposed that the NFR binds to the sub-domain IIA of HSA. Miraculously, all the results and information obtained by experimental and computational sections were compatible and confirmed each other. This valuable study and its valuable results owe good recorded experimental data and also owe using powerful computational approaches. This study may provide valuable information related the biological value and toxicity of NFR upon interaction with HSA.

## Acknowledgments

Gholivand M.B. and Jalalvand A.R. wish to express their sincere appreciation to Razi University Research Council for providing fund and time to do this project. Jalalvand A.R. was also supported by Kermanshah Oil Refining Company. Goicoechea H.C. thanks the UNL, CONICET and ANPCyT for financial support.

## Appendix A. Supplementary material

Supplementary data associated with this article can be found, in the online version, at http://dx.doi.org/10.1016/j.saa.2013.06.044.

## References

[1] I. Saha, J. Bhattacharyya, G.S. Kumar, J. Chem. Thermodyn. 56 (2013) 122.
[2] G. Wang, Do. Wang, X. Li, Y. Lu, Colloids Surf. B: Biointerfaces 84 (2011) 272.
[3] G. Wang, Ch. Yan, Y. Lu, Colloids Surf. B: Biointerfaces 106 (2013) 28.
[4] G. Wang, X. Li, X. Ding, D. Wang, Ch. Yan, Y. Lu, J. Pharm. Biomed. Anal. 55 (2011) 1223.
[5] X.M. He, D.C. Carter, Nature 358 (1992) 215.
[6] H.A. Tajmir-Riahi, J. Iran Chem. Soc. 3 (2006) 304.
[7] Y.V. Il'ichev, J.L. Perry, J.D. Simon, J. Phys. Chem. B 106 (2002) 459.
[8] Y.Y. Yue, X.G. Chen, J. Qin, X.J. Yao, J. Pharm. Biomed. Anal. 49 (2009) 759.
[9] J.S. Mandeville, E. Froehlich, H.A. Tajmir-Riahi, J. Pharm. Biomed. Anal. 49 (2009) 474.
[10] H.X. Luo, Y. Du, Z.X. Guo, Bioelectrochemistry 74 (2009) 235.
[11] Q.H. Lu, C.D. Ba, D.Y. Chen, J. Pharm. Biomed. Anal. 47 (2008) 891.
[12] C. Bertucci, V. Andrisano, R. Gotti, V. Cavrini, J. Chromatogr. B 768 (2002) 155.
[13] B. Bojko, A. Sulkowska, M. Maciazek-Jurczyk, J. Rownicka, W.W. Sulkowski, J. Mol. Struct. 924 (2009) 337.
[14] Y.N. Ni, S.S. Wang, S. Kokot, Anal. Chim. Acta 663 (2010) 146.
[15] Q. Zhang, Y.N. Ni, S. Kokot, Talanta 88 (2012) 532.
[16] M. Vives, R. Tauler, V. Moreno, R. Gargallo, Anal. Chim. Acta 446 (2001) 439.
[17] J. Jaumot, R. Eritja, R. Gargallo, Anal. Bioanal. Chem. 399 (2011) 1983.
[18] M. Vives, R. Gargallo, R. Tauler, Anal. Chem. 71 (1999) 4328.
[19] M. Vives, R. Gargallo, R. Tauler, Anal. Chim. Acta 424 (2000) 105.
[20] A. Alberich, C. Arino, J.M. Diaz-Cruz, M. Esteban, Anal. Chim. Acta 584 (2007) 403.
[21] M. Maeder, Anal. Chem. 59 (1987) 530.
[22] H. Gampp, M. Maeder, C.J. Meyer, A.D. Zuberbuhler, Talanta 32 (1985) 1139.
[23] A. de Juan, S. Navea, J. Diewok, R. Tauler, Chemom. Intell. Lab. Syst. 70 (2004) 21.
[24] S. Navea, A. de Juan, R. Tauler, Anal. Chem. 74 (2002) 6039.
[25] http://www.arguslab.com.
[26] A.C. Wallace, R.A. Laskowski, J.M. Thornton, Protein Eng. 8 (1995) 134.
[27] R. Vandrunen, Comput. Phys. Commun. 91 (1995) 56.
[28] E. Lindahl, B. Hess, J. Mol. Model. 7 (2001) 317.
[29] http://www.ub.es/gesq/mcr/mcr.htm.
[30] J.R. Lakowicz, Principles of Fluorescence Spectroscopy, third ed., Springer, New York, 2006.
[31] M.A. Khan, S. Muzammil, J. Musarrat, Int. J. Biol. Macramol. 30 (2002) 249.
[32] G. Sudlow, D.J. Birkett, D.N. Wade, Mol. Pharmacol. 12 (1976) 1061.
[33] Y.N. Ni, Y.H. Lai, S. Brandes, S. Kokot, Anal. Chim. Acta 647 (2009) 158.
[34] G. Munoz, A. de Juan, Anal. Chim. Acta 595 (2007) 208.
[35] J.R. Lakowicz, G. Weber, Biochemistry 12 (1973) 4170.
[36] Y.J. Hu, Y. Liu, X.H. Xiao, Biomacromolecules 10 (2009) 521.
[37] H. Zhang, X. Huang, M. Zhang, Mol. Biol. Rep. 35 (2008) 705.
[38] F. Ding, L. Zhang, J. Diao, X. Li, L. Ma, Y. Sun, Ecotoxicol. Environ. Saf. 79 (2012) 246.
[39] I.M. Klotz, Ann. N. Y. Acad. Sci. 226 (1993) 35.
[40] F. Samari, M. Shamsipur, B. Hemmateenejad, T. Khayamian, S. Gharaghani, Eur. J. Med. Chem. 54 (2012) 263.
[41] L. Stryer, R.P. Haugland, Proc. Natl. Acad. Sci. USA 58 (1967) 726.
[42] B. Valeur, J.C. Brochon, New Trends in Fluorescence Spectroscopy, third ed., Springer, Berlin, 2001.
[43] F.L. Cui, J. Fan, J.P. Li, Z.D. Hu, Bioorg. Med. Chem. 12 (2004) 157.
[44] H. Heli, N. Sattarahmady, A. Jabbari, A.A. Moosavi-Movahedi, G.H. Hakimelahi, F.-Y. Tsai, J. Electroanal. Chem. 610 (2007) 74.
[45] R.M. Dyson, S. Kaderli, G.A. Lawrance, M. Maeder, A.D. Zuberbühler, Anal. Chim. Acta 353 (1997) 393.